MHz - Tomoscopy

D3.2

Report on the simulations of cavitation peening

Project information

Project full title	MHz rate mulTiple prOjection X-ray MicrOSCOPY
Project acronym	MHz-TOMOSCOPY
Grant agreement no.	101046448
Instrument	EIC Pathfinder Open
Duration	42 months
Website	https://tomoscopy.eu/

Deliverable information

Deliverable no.	D3.2
Deliverable title	Report on the simulations of cavitation peening
Deliverable responsible	UOXF
Related Work-Package/Task	Task 3.2
Type (e.g. report; other)	Report
Author(s)	Mohammad Shahsavari and Daniel Eakins
Dissemination level	public
Document Version	1.0

Funded by
the European Union

Date	12/30/2024
Download page	

Document information

Version no.	Date	Author(s)	Comment
V1	11/30/2024	Mohammad Shahsavari and Daniel Eakins	-

Funded by
the European Union

Abstract

In Task 3.2, we developed a numerical strategy and two numerical solvers–a cost-efficient code and an advanced code–to simulate cavitating flows. These codes have undergone extensive validation against theoretical predictions and data from the literature. We used these numerical tools to select and tailor sample environments for the MHz X-ray microscopy. The results were also fed into the ML algorithm developed in Task 2.3. This document provides an overview of the codes developed for simulating the fluid flow phase in cavitation peening, their validation processes, and numerical results for selected sample environments.

Executive Summary

In deliverable D3.2, we report on the simulations of cavitation peening related to Task 3.2, in which we developed advanced numerical codes to predict the multi-phase interaction (liquid-gas and liquid-solid) in the cavitation peening process. These codes have been used to explore various aspects of cavitation peening. The obtained results will be refined and validated after collecting the MHz X-ray microscopy data (Task 3.4) and will be used as input for the ML algorithm developed in Task 2.3.

Funded by
the European Union

Table of Contents

Funded by
the European Union

Introduction

Cavitation refers to the formation of vapor bubbles in liquids when the local liquid pressure drops below the vapor pressure [1]. These structures collapse violently, generating short-duration, high-amplitude pressure waves as the flow recovers its pressure [1]. These pressure waves can enhance material fatigue life by inducing compressive residual stresses that delay crack growth, a process known as cavitation peening [2]. Cavitation involves complex physical phenomena, including shock waves and hydrodynamic features, spanning broad ranges of spatial and temporal scales. Resolving these features requires accurate numerical methodologies and significant computational resources. In Task 3.2, we developed, validated, and applied numerical codes to investigate cavitation peening.

It is known that the mutual effects of the solid phase on fluid flow in cavitation peening are negligible because the length scale of pits produced in materials by cavitation is significantly smaller than the length scale of the hydrodynamic features in the flow field [3]. Therefore, the modeling process can be decoupled: the fluid flow is simulated first, and the results are subsequently used to model the peening process using solid mechanics numerical platforms. Following this approach, we developed numerical tools to simulate the fluid flow to meet the core objectives of Work Package 3. After calculating the forces exerted by fluid flow on solid surfaces, we employed codes developed by the Impact and Shock Mechanics Research Group at the University of Oxford to assess the effects of these forces on material specification.

The developed numerical tools for fluid flow consist of an advanced, yet computationally expensive code and a cost-efficient solver. The advanced code employs the density-based approach, capturing all flow features, including acoustic waves, by restricting the numerical resolution to be significantly smaller than the smallest flow time scale. In contrast, the cost-efficient code uses the pressure-based approach, incorporating fluid compressibility in the pressure-velocity coupling. This allows for a coarser numerical resolution compared to the advanced code, making it a suitable option for large parameter scans and sensitivity analyses.

In this report, we briefly introduce the numerical tools, their validation processes, and some of our investigations into cavitation and the tailoring of sample environments for MHz X-ray microscopy.

Numerical Codes

Cost-efficient code

In this code, we used the single fluid mixture model, in which both vapor and liquid phases are treated using one set of Navier-Stokes equations, which has been proven accurate in predicting complex features of cavitation [4-6]. The governing equations used in this solver are as below,

$$\frac{\partial \rho}{\partial t} + \frac{\partial (\rho u_k)}{\partial x_k} = 0, \quad (1)$$

$$\frac{\partial(\rho u_i)}{\partial t} + \frac{\partial(\rho u_i u_k)}{\partial x_k} = -\frac{\partial(p\delta_{ik})}{\partial x_k} + \frac{\partial}{\partial x_k}\left[\mu\left(\frac{\partial u_i}{\partial x_j} + \frac{\partial u_j}{\partial x_i} - \frac{2}{3}\frac{\partial u_k}{\partial x_k}\delta_{ij}\right)\right], \quad (2)$$

$$\frac{\partial(\rho Y)}{\partial t} + \frac{\partial(\rho Y u_k)}{\partial x_k} = S_e - S_c, \quad (3)$$

where u is the velocity, ρ is the mixture density, p is the pressure, μ is the viscosity, Y is the vapour mass fraction, and δ_{ik} is the Kronecker delta. Here, the PIMPLE algorithm [7] was used to couple the pressure and velocity while considering the fluid compressibility. In Eq. 3, S_e and S_c are the evaporation and condensation source terms, respectively, evaluated using the following expressions proposed by Saito *et al.* [8, 9],

$$S_e = C_e\alpha^2(1-\alpha)^2\frac{\rho_l}{\rho_g}\frac{max((p_{sat}-p),0)}{\sqrt{2\pi R_g T_{ref}}}, \quad (4)$$

$$S_c = C_c\alpha^2(1-\alpha)^2\frac{max((p_{sat}-p),0)}{\sqrt{2\pi R_g T_{ref}}}, \quad (5)$$

where C_e and C_c are the model constants, α is the vapour volume fraction, ρ_l is the liquid density, ρ_g is the gas density, p_{sat} is the saturated pressure, R_g is the gas constant, and T_{ref} is the reference temperature. Here, C_e and C_c were set to 0.1, proven to be an optimum value to determine the mass transfer through evaporation and condensation [8].

In this solver, the mixture density and viscosity were defined as,

$$\rho = \alpha\rho_{v,sat} + (1-\alpha)\rho_{l,sat}, \quad (6)$$

$$\mu = \alpha\mu_v + (1-\alpha)\mu_l, \quad (7)$$

where $\rho_{v,sat}$ is the saturated vapor density, μ_v is the vapour viscosity, $\rho_{l,sat}$ is the saturated liquid density, and μ_l is the liquid viscosity. Additionally, α is related to Y by,

$$\rho_g\alpha = \rho Y, \quad (8)$$

where ρ_g was obtained by using the barotropic equation of state namely,

$$c_v^2 = \left.\frac{\partial p}{\partial \rho_g}\right|_s, \quad (9)$$

where c_v is the sound speed in the vapor. Here, the liquid density was calculated by,

$$\rho_l = \rho_{l,sat} + \frac{p}{\rho c_l^2}, \quad (10)$$

where c_l is the sound speed in the pure liquid [4]. In this code, fluid properties were obtained at a constant T_{ref} while employing the barotropic equation of state alongside a model to estimate the sound speed in the mixture, c_m. We conducted preliminary studies to assess the accuracy of the available sound speed expressions for the mixture, including linear, equilibrium, and frozen models [10]. In the linear model, presented as follows, c_m is a linear function of α, c_v, and c_l.

$$\frac{1}{c_m^2} = \frac{\alpha}{c_v^2} + \frac{1-\alpha}{c_l^2}. \tag{11}$$

In the equilibrium model, it is assumed that the heat transfer between the phases is infinitely fast, and the phases are in equilibrium thermodynamically. Therefore, the latent heat of vaporization, L_v, is included in the calculation of c_m using,

$$\frac{1}{\rho c_m^2} = \frac{\alpha}{\rho_{v,sat} c_v^2} + \frac{1-\alpha}{\rho_{l,sat} c_l^2} + \frac{(1-\alpha)\rho_{l,sat} C_{pl} T}{\left(\rho_{v,sat}\, L_v\right)^2}, \tag{12}$$

where C_{pl} is the specific heat of the liquid phase at constant pressure and T is the temperature. In contrast, in the frozen model, the heat transfer between the phases is assumed to be infinitely slow, resulting in the following expression,

$$\frac{1}{\rho c_m^2} = \frac{\alpha}{\rho_{v,sat} c_v^2} + \frac{1-\alpha}{\rho_{l,sat} c_l^2}. \tag{13}$$

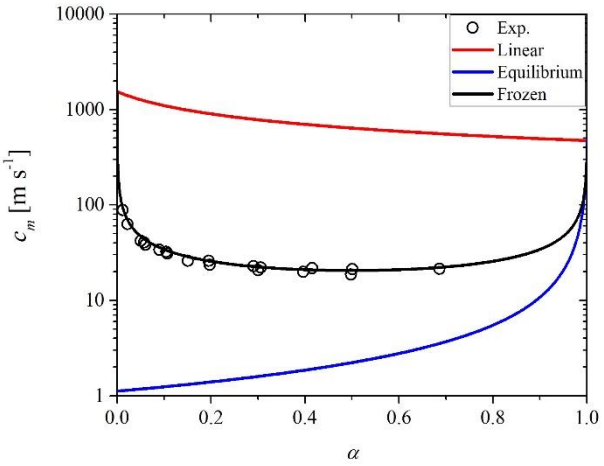

Fig 1. Comparison of the speed of sound in water-air mixture as a function of vapor volume fraction predicted by linear, equilibrium, and frozen models to the experimental data by Karplus, Gouse and Brown [11, 12].

We evaluated the performance of these models by reproducing the experimental data of Karplus, Grouse and Brown published for water-air mixtures at 1 atm [11, 12]. The results presented in Fig. 1, show that the linear model significantly over-predicts the sound speed, whereas the equilibrium model under-predicts it. According to Fig. 1, the frozen model closely matches the experimental data. Therefore, the frozen model was employed in the codes to calculate the speed of sound in mixtures.

In this solver, we used a four-step Runge-Kutta scheme for temporal discretization while keeping the Courant-Friedrichs-Lewy, *CFL*, calculated based on the sound speed to be less than 0.7. Moreover, we employed Gaussian TVD schemes to discretize the spatial terms.

Advanced code

In this code, we add the following energy equation to the set of governing equations presented in Eqs. 1-3,

$$\frac{\partial(\rho E)}{\partial t}+\frac{\partial(\rho(E+p)u_k)}{\partial x_k}=\frac{\partial}{\partial x_k}\left[\mu\left(\frac{\partial u_i}{\partial x_j}+\frac{\partial u_j}{\partial x_i}-\frac{2}{3}\frac{\partial u_k}{\partial x_k}\delta_{ij}\right)u_i\right]+\frac{\partial}{\partial x_k}\left(\lambda\frac{\partial T}{\partial x_i}\right), \quad (14)$$

where E is the total energy and λ is the thermal conductivity. Unlike in the pressure-based solver, here, the evaporation and condensation source terms in Eq. 3 were evaluated using the calculated temperature instead of T_{ref}. We used Eq. 13 to calculate the sound speed in the mixture and obtained the sound speed in the vapor and liquid using the ideal gas law and the following correlation by Wilson [13], respectively,

$$c_l=a_0+a_1T+a_2T^2+a_3T^3+a_4T^4, \quad (15)$$

where T is in [˚C], and a_i are defined as,

$$a_i=\sum_{j=0}^{3}b_{ij}p^j, \quad (16)$$

where p is in [psia] and b_{ij} are the model constants presented in Table 1.

Table 1. Model constants for the calculation of sound speed in liquid water [13].

		b_{ij}			
		$j=0$	$j=1$	$j=2$	$j=3$
a_i	$i=0$	1402.859	1.050469×10^{-2}	1.633786×10^{-7}	-3.889257×10^{-12}
	$i=1$	5.023859	6.138077×10^{-5}	-1.080177×10^{-8}	2.477679×10^{-13}
	$i=2$	-5.690577×10^{-2}	-1.071154×10^{-6}	2.215786×10^{-10}	-5.088886×10^{-15}
	$i=3$	2.884942×10^{-4}	1.582394×10^{-8}	-2.420956×10^{-12}	5.086237×10^{-17}
	$i=4$	-8.238863×10^{-7}	-6.839540×10^{-11}	9.711687×10^{-15}	-1.845198×10^{-19}

The saturated densities and pressure required by Eqs. 4, 5, and 13 were obtained employing the following correlations by Wagner and Pruss [14],

$$p_{sat}=p_{cr}\times exp\left[\left(\frac{T_{cr}}{T}\right)\left(a_0T_r+a_1T_r^{3/2}+a_2T_r^{6/2}+a_3T_r^{7/2}+a_4T_r^{8/2}+a_5T_r^{15/2}\right)\right], \quad (17)$$

$$\rho_{l,sat}=\rho_{cr}\left[1+b_0T_r^{1/3}+b_1T_r^{2/3}+b_2T_r^{5/3}+b_3T_r^{16/3}+b_4T_r^{43/3}+b_5T_r^{110/3}\right], \quad (18)$$

$$\rho_{v,sat}=\rho_{cr}\left[c_0T_r^{2/6}+c_1T_r^{4/6}+c_2T_r^{8/6}+c_3T_r^{18/6}+c_4T_r^{37/6}+c_5T_r^{71/6}\right], \quad (19)$$

where

$$T_r=1-\frac{T}{T_{cr}}, \quad (20)$$

and T_{cr} is the critical temperature, p_{cr} is the critical pressure, and ρ_{cr} is the critical density of water, which are 647.096 K, 22.064 MPa and 322 kg m^{-3}, respectively. Moreover, a_i, b_i, and c_i are the model constants presented in Table 2.

Funded by the European Union

Table 2. Model constants for saturated density and pressure calculations [14].

	a_i, b_i, and c_i					
	$i = 0$	$i = 1$	$i = 2$	$i = 3$	$i = 4$	$i = 5$
p_{cr}	-7.85951783	1.84408259	-11.7866497	22.6807411	-15.9618719	1.80122502
$\rho_{l,sat}$	1.99274064	1.09965342	-0.510839303	-1.75493479	-45.5170352	-6.7469445×10^{5}
$\rho_{v,sat}$	-2.0315024	-2.6830294	-5.38626492	-17.2991605	-44.7586581	-63.9201063

In this solver, the mixture properties were defined as,

$$\rho = \alpha\rho_v + (1-\alpha)\rho_l, \tag{21}$$

$$\mu = \alpha\mu_v + (1-\alpha)\mu_l, \tag{22}$$

$$\lambda = \alpha\lambda_v + (1-\alpha)\lambda_l. \tag{23}$$

The vapor and liquid properties, namely density, viscosity, thermal conductivity and heat capacities at constant pressure and density, were determined by fitting polynomials to the NIST database. Moreover, the stiffened equation of state [9] was used to relate the state variables,

$$p = Y\rho R_g T + (1-Y)\rho K_l T\frac{p}{p+p_c}, \tag{24}$$

where K_l = 2684.075 J kg^{-1} K^{-1} and p_c = 786.33×10^6 Pa.

In this solver, we calculated the numerical fluxes by employing the HLLC-AUSM Riemann solver [15] and the limiter proposed by Barth and Jespersen [16]. Furthermore, we used a four-step Runge-Kutta scheme to discretize the temporal terms while setting the maximum value of the *CFL* number at 0.2. Comparing the required *CFL* numbers, the density-based code is 3.5 times more expensive than the pressure-based code.

Validations

The numerical solvers were validated by simulating two benchmarks: a single bubble collapse and a bubble cluster collapse near a flat wall.

The first benchmark involves an unbounded spherical vapor bubble of radius R_0 = 0.4 mm at the center of a large spherical domain with a radius of 1250 R_0 filled with water. Here, we simulated an octant of this domain considering the spherical symmetry of the flow field. Figure 2 shows the schematic of this benchmark. We meshed this domain using Cartesian structured grids using two numerical grids, coarse and fine, to assess the sensitivity of the results to the grid size. In the coarse grid, the cell size, Δ, was 20 µm near the bubble, while the corresponding size in the fine grid was 10 µm, corresponding to R_0/Δ of 20 and 40, respectively. At the far field boundary shown in Fig. 2, the pressure was fixed at 101325 Pa. Furthermore, the symmetry boundary condition was used for all other boundaries. The domain was initially filled with liquid water at 298.15 K and 101325 Pa. The water pressure around the bubble had a Laplacian distribution at the initial

Funded by the European Union

condition. The vapor pressure and density inside the bubble were initially set at p_{sat}= 3170 Pa and 0.023075 kg m^{-3}, respectively.

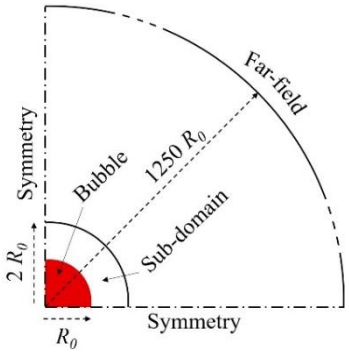

Fig 2. Schematic of the computational domain used for simulating single bubble collapse.

Figure 3 shows the temporal evolution of the bubble radius, *R*, using the pressure- and density-based solvers with two numerical grids. The numerical simulation results are also compared with the analytical solution proposed for this benchmark [17], which derives the temporal evolution of the bubble radius as,

$$\frac{dR}{dt} = -\left(\frac{2}{3}\frac{p_\infty - p_v}{\rho}\left(\left(\frac{R_0}{R}\right)^3 - 1\right)\right)^{1/2}, \tag{25}$$

where p_∞ is the far field (ambient) pressure and p_v is the vapour pressure. The latter is set equal to p_{sat} in the present simulations. In Fig. 3, the bubble radius is non-dimensionalized with R_0 and time, *t*, is non-dimensionalized by the analytical value of the collapse time, τ_R, given by,

$$\tau_R = 0.915 R_0 \left(\frac{\rho}{p_\infty - p_v}\right)^{1/2}. \tag{26}$$

The results show that both solvers predict the analytical results well. Furthermore, the results show that meshing an unbounded bubble with 20 cells in the radial direction is sufficient to resolve the bubble evolution.

In the second benchmark, depicted in Fig. 4, we simulated a cloud of bubbles collapsing near a flat wall. The cloud consists of 125 bubbles with radii ranging from 0.7 to 1.64 mm, selected randomly while keeping the average radius at 0.95 mm. These bubbles were distributed in a cubic domain of $21R_c \times 21R_c \times 21R_c$, inscribed in a large rectangle of $4200R_c \times 4200R_c \times 2100R_c$. The large bubbles were placed at the center of the cloud. Furthermore, the minimum distance between two adjacent bubbles was 0.2 mm to prevent any intersections between the bubbles. The domain was filled with liquid water at 293.15 K and 4 MPa with a density of 998.16 kg m^{-3} and viscosity of 0.001 kg m^{-1}s^{-1}. The vapor pressure was equal to the saturated pressure, p_{sat}= 2340 Pa. Pressure at far-field boundaries was maintained at 4 MPa, while the zero gradient boundary condition was used for density, velocity, temperature, viscosity, and vapor mass fraction. Moreover, the bottom boundary was treated as a wall. The computational domain was meshed using non-uniform Cartesian structured cells. The cell size was uniform in the small sub-domain with Δ = 0.1 mm while gradually stretched out within the large domain.

Funded by
the European Union

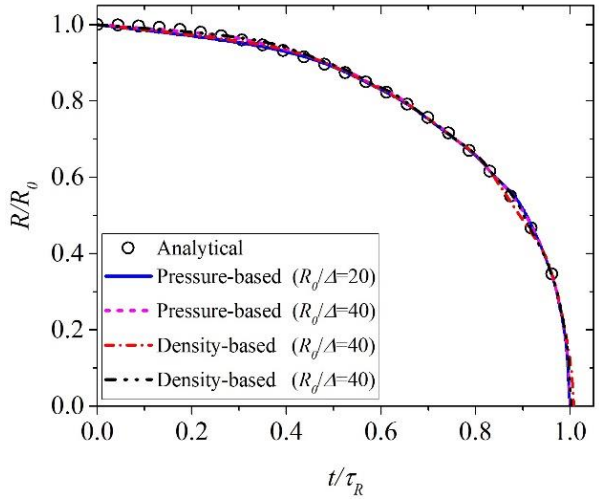

Fig 3. Temporal evolution of the bubble radius predicted by analytical solution and numerical simulations.

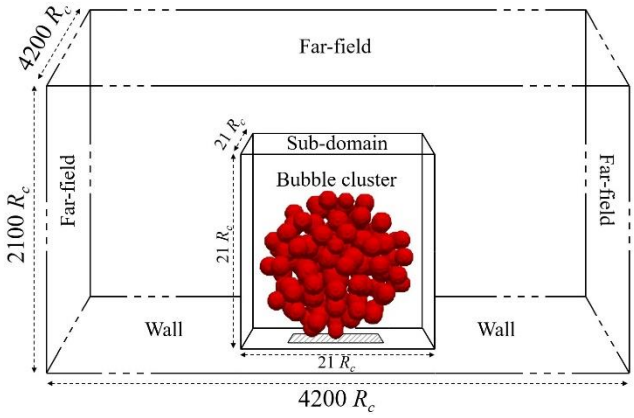

Fig 4. Schematic of the computational domain and the initial distributions of the bubbles. R_c is the average radius of the bubbles in this cloud.

This benchmark has been used by Ghahramani *et al.* and Schmidt *et al*. to verify numerical solvers [6, 18]. Figure 5 shows the impact pressure by the bubble cluster collapse on the wall predicted by the present simulations and those from Ghahramani *et al.* and Schmidt *et al.* [6, 18]. The legend provides the cell size used in each simulation. The pressure was measured by taking the average pressure over an area of 10×10 mm^2 of the wall beneath the cloud, the hatched surface in Fig. 4. The results demonstrate that the impact pressure predicted by the present solvers is in the range of those reported in the literature [6, 18]. Discrepancies are believed to be caused by bubble distributions at the initial condition.

Funded by
the European Union

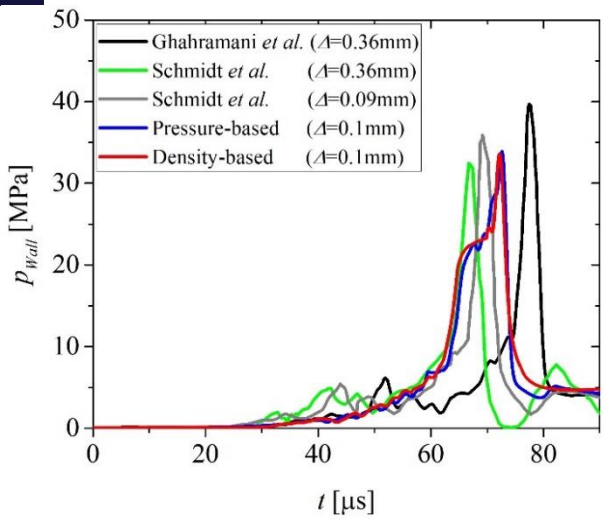

Fig 5. Impact pressure by the collapse of the bubble cluster over an area of 10×10 mm^2 of the wall beneath the cloud.

Results

As the first sample environment, we focused on cavitation peening through hydrodynamic cavitation within nozzles and narrow channels. The objective was to characterize vortex cavitation and identify its origin. It is believed that these coherent cavitating structures are responsible for producing abrupt collapses that release strong shock waves [19]. Figure 6 (a) shows a snapshot of vortex cavitation formed in a rectangular nozzle obtained using the cost-efficient code. The cavitating regions are illustrated by plotting the iso-surface of the vapor volume fraction at 0.1. Furthermore, Fig. 6 (b) shows an iso-surface of the vorticity magnitude, highlighting the turbulent coherent structures. A comparison of Figs. 6 (a) and (b) reveals that the horseshoe vortex turbulent structures, generated near solid boundaries close to the nozzle throat, coincide with the location of vortex cavitation. This indicates that horseshoe vortices are probably responsible for forming vortex cavitation by reducing the local pressure below the saturated pressure.

We used the obtained numerical results to evaluate whether the spatiotemporal characteristics of vortex cavitation fall within the resolution of the MHz X-ray microscopy. To this end, we placed several numerical probes near the solid boundaries and collected velocity and pressure signals. Post-processing of these signals revealed that the length scale of vortex cavitation is on the order of millimeters, while its time scale is approximately one millisecond. These characteristics are significantly larger than the resolution of the MHz X-ray microscopy, as listed in Table 3. This implies that resolving these structures with MHz X-ray microscopy would require extensive experimental scans to discern vortex cavitation.

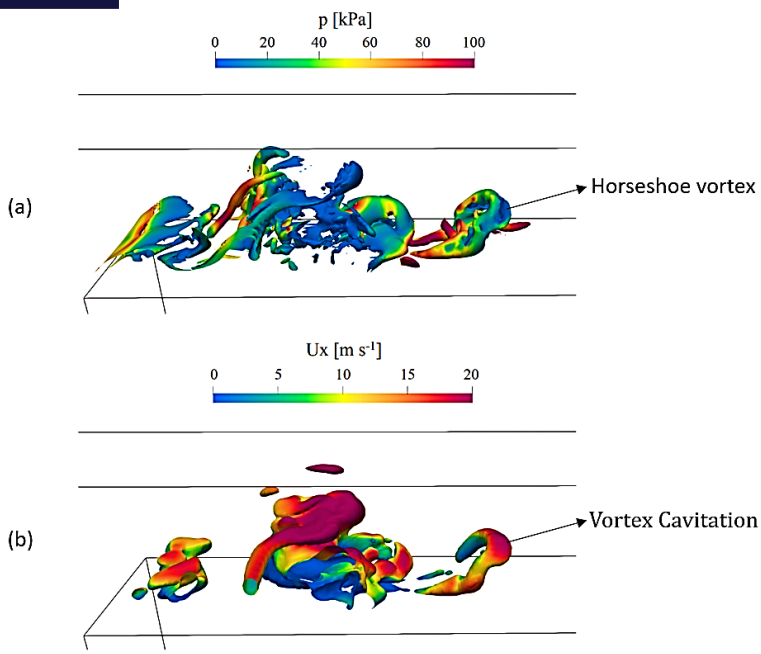

Fig 6. Iso-surfaces of (a) the vapor volume fraction, color-coded by local pressure, and (b) vorticity magnitude, color-coded by the flow velocity.

Table 3. MHz X-ray microscopy resolution.

Continuous Recording Capacity [frame]	128
Recording Speed [Mega frame per second]	1.1
Recording duration [microsecond]	116
Field of View [millimeter]	0.8-1.3

Following similar analyses for different nozzles and the study of various physical phenomena, such as cavitation inception and pulsing cavitation, we concluded that sample environments involving hydrodynamic cavitation are not suitable for MHz X-ray microscopy measurements. Preliminary numerical studies revealed that the resolution of this novel technique falls in the spatiotemporal characteristics of cavitation peening via cavitation bubbles. In this form of cavitation peening, a small bubble is generated near a material by discharging a laser pulse into the liquid. The resulting significant pressure gradient across the bubble interface drives its implosion, releasing strong shock waves. These shocks introduce compression stress in the material, leading to surface pits. This technique has been proven effective for peening various materials [20]. However, the dynamics of bubble collapse remain poorly understood, as they involve small spatial and temporal scales that are beyond the reach of conventional measurement techniques.

Theoretically, as indicated by Eq. 26, the lifetime of a cavitation bubble is proportional to its initial size and the thermodynamic conditions of the flow. This suggests that cavitation bubbles can be easily tailored to match the resolution of MHz X-ray microscopy, making this sample environment well-suited for this project. Moreover, the generation and collapse of cavitation bubbles using lasers are highly controllable and can be synchronized with the measurement technique, minimizing the experimental scans needed to capture the targeted features.

Funded by
the European Union

We used the numerical codes to characterize cavitation bubble dynamics, focusing on identifying key features during the bubble collapse for further investigations with MHz X-ray microscopy. Simulations were performed for cavitation bubbles in water near a flat wall under a broad range of thermodynamic conditions. Figure 7 shows a schematic of one such simulation, where a spherical water vapor bubble is generated above a flat wall. Figure 8 illustrates the spatial distributions of pressure (non-dimensionalized by the liquid pressure) and the velocity component perpendicular to the wall (u_z) at a cross-section of the computational domain. Here, the bubble shape is indicated by iso-lines of α (white lines) superimposed on the velocity and pressure contours. Additionally, the closed black line in Fig. 8 (a) shows the initial bubble shape.

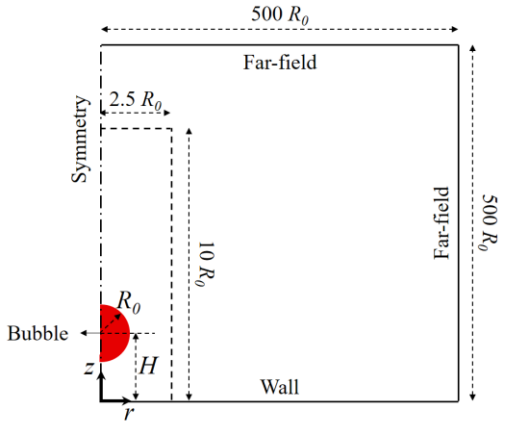

Fig 7. Schematic of the computational domain used to study cavitation bubble above a flat surface.

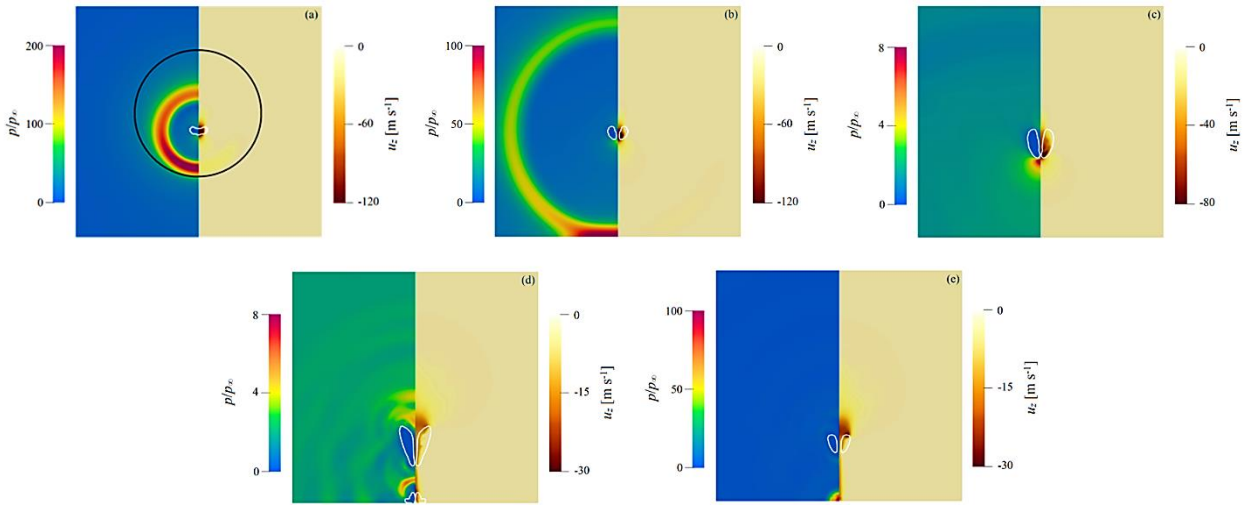

Fig 8. Spatial distributions of the pressure (left of each panel) and velocity component perpendicular to the wall (right of each panel) at a cross-section of the computational domain at t/τ_R values of (a) 1.002, (b) 1.01, (c) 1.05, (d) 1.7, and 1.74. The closed white and black lines show the current and initial shapes of the bubble, respectively.

The results show that the bubble shrinks for $t/\tau_R < 1$, remaining nearly symmetric during this phase. The pressure below the bubble is lower than the above due to the influence of the solid boundary, creating an asymmetrical pressure distribution. This asymmetry generates a re-entrant jet directed toward the wall, causing the bubble to elongate and move closer to the surface. As the re-entrant jet pierces the bubble early in its collapse, the bubble transforms into

Funded by
the European Union

a bowl-like structure (Fig. 8 (a)) and subsequently evolves into a toroidal shape (Fig. 8 (b)). After the first collapse, an outward-propagating compression wave generates a low-pressure region, prompting the bubble to re-evolve. The re-entrant jet then impinges on the surface, exerting another impact pressure. Following this, as displayed in Fig. 8 (d), the elongated bubble fragments into pieces. The wall-attached bubble collapses before the detached bubble, as seen in Fig. 8 (e), imposing additional impact pressures on the surface.

These analyses show that cavitation bubbles exhibit complex physical features with small spatiotemporal scales, making them a suitable sample environment for MHz X-ray microscopy. Many of these phenomena, particularly those occurring after the first collapse ($t/\tau_R > 1$), are not understood well. These features directly influence the impact pressures and the effectiveness of cavitation peening. In Task 3.4, the MHz X-ray microscopy technique will be used to gather data for validating the obtained numerical results. Additionally, the developed models and the obtained results have been prepared into a journal paper, which will be submitted shortly.

Conclusions

In Task 3.2, we developed two numerical solvers with varying computational demands: a cutting-edge yet resource-intensive code and a low-cost solver to simulate cavitating flows. Using a density-based approach, the former code resolves all the flow characteristics, including acoustic waves, with small numerical steps. In comparison, the cost-effective code is based on the pressure-based approach while considering the fluid compressibility in the pressure-velocity coupling, being stable for relatively large computational time steps. These codes were successfully validated against theoretical predictions and data from the literature. We used these codes to select and optimize the sample environments for the MHz X-ray microscopy, namely cavitating nozzles and cavitation bubbles. The obtained results were fed into the ML algorithm developed in Task 2.3.

References

[1] C. Brennen, Cavitation and bubble dynamics, Oxford University Press, 1995.

[2] H. Soyama and A. Korsunsky, "A critical comparative review of cavitation peening and other surface peening methods," *Journal of Materials Processing Technology,* vol. 305, no. 117586, 2022.

[3] H. Soyama and Y. Iga, "Laser cavitation peening: a review," *Applied Science,* vol. 13, No. 11, 2023.

[4] D. Zhao, L. Zhang, F. Deng, P. Moin, Y. Li and S. X., "A comparative study of the impact pressure induced by a single cavitation bubble collapsing near a solid wall," *Physics of Fluids,* vol. 36, p. 073327, 2024.

[5] B. Budich, S. Schmidt and N. Adams, "Numerical simulation and analysis of condensation shocks in cavitating flow," *Journal of Fluid Mechanics,* vol. 838 , pp. 759-813, 2018.

[6] E. Ghahramani, M. Arabnejad and R. Bensow, "A comparative study between numerical methods in simulation of cavitating bubbles," *International Journal of Multiphase Flow,* vol. 111, pp. 339-359, 2019.

[7] I. Barton, "Comparison of SIMPLE- and PISO-type algorithms for transient flows," *International Journal for Numerical Methods in Fluids,* vol. 26, pp. 459-483, 1998.

[8] Y. Saito, R. Takami, I. Nakamori and T. Ikohagi, "Numerical analysis of unsteady behaviour of cloud cavitation around a NACA0015 foil," *Computational Mechanics,* vol. 40, pp. 85-96, 2007.

[9] A. Gnanaskandan and K. Mahesh, "A numerical method to simulate turbulent cavitating flows," *International Journal of Multiphase Flow,* vol. 70, pp. 22-34, 2015.

[10] G. Wallis, One-dimensional two-phase flow, McGraw-Hill, 1969.

[11] H. Karplus, "Velocity of sound in a liquid containing gas bubbles," *The Journal of the Acoustical Society of America,* vol. 29, no. 1261, 1957.

[12] S. Grouse and J. Brown, "A survey of the velocity of sound in two-phase mixtures," *ASME paper,* no. 64-WA/FE-35, 1964.

[13] W. Wilson, "Speed of sound in distilled water as a function of temperature and pressure," *The Journal of the Acoustical Society of America,* vol. 31, no. 8, 1959.

[14] W. Wagner and A. Pruss, "International equations for the saturation properties of ordinary water substance. Revised according to the international temperature scale of 1990," *Journal of Physical and Chemical Reference Data,* vol. 16, no. 893, 1987.

[15] A.H. Koop "Numerical simulation of unsteady three-dimensional sheet cavitation," Ph.D. thesis, University of Twente, 2008.

[16] T.J. Barth and D.C. Jespersen, "The design and application of upwind schemes on unstructured meshes," *27th Aerospace Sciences Meeting*, American Institute of Aeronautics and Astronautics, Paper 0366, 1989.

[17] J. Franc and J. Michel, Fundamentals of cavitation, Springer Science and Business Media, 2006.

[18] S. Schmidt, M. Mihatsch, M. Thalhamer and N. Adams, "Assessment of erosion sensitive area via compressible simulation of unsteady cavitating flows," in *Advanced experimental and numerical techniques for cavitation erosion prediction*, Springer , 2014.

[19] H. Soyama, X. Liang, W. Yashiro, K. Kajiwara, E.M. Asimakopoulou, V. Bellucci, S. Birnsteinova, G. Giovanetti, C. Kim, H.J. Kirkwood, J.C.P. Koliyadu, R. Letrun, Y. Zhang, J. Uličný, R. Bean, A.P. Mancuso, P. Villanueva-Perez, T. Sato, P. Vagovič, D. Eakins, A.M. Korsunsky, "Revealing the origins of vortex cavitation in a Venturi tube by high speed X-ray imaging," *Ultrasonics Sonochemistry*, vol. 101, no. 106715, 2023.

[20] A. Philipp and W. Lauterborn, “Cavitation erosion by single laser-produced bubbles,” *Journal of Fluid Mechanics,* vol. 361, pp. 75-116, 1998.

Funded by
the European Union